Journal of Materials Chemistry A

COMMUNICATION

View Article Online
View Journal | View Issue

Cite this: J. Mater. Chem. A, 2017, 5, 8261

Received 25th January 2017
Accepted 14th April 2017

DOI: 10.1039/c7ta00842b

rsc.li/materials-a

Spatial selectivity of photodeposition reactions on polar surfaces of centrosymmetric ferroelastic γ-WO_3†

Ajay S. Pisat, Gregory S. Rohrer and Paul A. Salvador *

Two of three levels of hierarchical ferroelastic domains of γ-WO_3 ceramics are shown to be piezo-responsive (polar) for surfaces of any general orientation. Importantly, the surface activity for the photocathodic reduction of Ag^+ and photoanodic oxidation of Pb^{2+}/Mn^{2+} ions is correlated to those same two levels of ferroelastic domains for all orientations.

Carbon dioxide (CO_2) emissions from continued use of traditional energy sources are leading to irreversible climate change.[1] The development of clean (CO_2 neutral) energy sources might mitigate the effects of energy use on climate.[2] Hydrogen (H_2) does not produce CO_2 on combustion,[3] but H_2 production by steam-reforming produces 9–12 tons of CO_2 for every ton of H_2.[4] Photocatalytic water splitting, or the conversion of H_2O to H_2 and O_2 using catalysts and the energy in light, is a CO_2-free method for H_2 production. Though photocatalytic water splitting was first studied in 1972,[5] the economically viable production of H_2 by photocatalytic water splitting still eludes us because of a lack of high efficiency, cost effective catalysts.[6]

Separation of photogenerated charge carriers is a key challenge in the development of photocatalysts with high internal quantum efficiencies (IQEs).[7] Glickstein *et al.*[8,9] computed a maximum IQE of almost 90% for ferroelectric photocatalysts, which have natural polar domains in the absence of applied fields. Because only 10 of 32 point groups support ferroelectricity,[10,11] the number of naturally polar crystals is limited. Further, most ferroelectrics are wide band gap dielectrics that do not absorb enough of the solar spectrum to operate as solar water splitting catalysts.[12–14]

Recently, Munprom *et al.*[15,16] showed that ferroelastic domains at the surface of polycrystalline centrosymmetric monoclinic (m-) $BiVO_4$ were polar and promoted spatial selectivity of oxidation and reduction reactions in a similar fashion to ferroelectrics.[14,17,18] It was proposed that the polar surface domains in m-$BiVO_4$ were of flexoelectric origin, in which a polarization develops from a strain gradient.[19] Strain gradients could arise from residual surface and/or ferroelastic transformation strains.[15,16] Charge carrier separation from flexoelectricity is interesting because flexoelectricity is not limited by structural symmetry; materials of all point groups can be flexoelectric.[19] Even if the effect is related to the ferroelastic nature of m-$BiVO_4$, ferroelastics are abundant, making up more than 30% of the Earth's crust.[20] It is therefore of interest to establish whether polar surfaces in other ferroelastics promote separation of carriers and reactions.

Like $BiVO_4$,[21,22] WO_3 is a widely researched photocatalyst for water splitting.[23–27] γ-WO_3 is centrosymmetric with a band gap of 2.6 eV,[28,29] and thus is photocatalytically active in visible light.[24,25] WO_3 adopts different crystal structures as a function of temperature, all related to displacive distortions of the pseudo-perovskite ReO_3 structure (for which the A-site of the cubic perovskite ABO_3 structure is unoccupied).[28,30–37] The sequence of phase transitions is discussed elsewhere.[28,30–37] Those relevant to this work are the transformations above room temperature: tetragonal (α) WO_3 transforms to orthorhombic (β) at ≈740 °C, and β-WO_3 transforms to monoclinic (γ) at ≈310 °C (other transformations occur below room temperature[28,30–33,38]). The α–β and β–γ transformations (which happen on cooling during synthesis) are ferroelastic.[39–43] The ferroelastic domain structures in γ-WO_3 are known to be complex and hierarchical, and can evolve with time or stress.[39–46] Interestingly, Kim *et al.*[47] demonstrated that the surface layer in heavily reduced single crystals of WO_3 is piezoresponsive. More recently, hierarchical domain structures were found in epitaxial γ-WO_3 thin films, and one level of domains was shown to be piezoresponsive (polar).[44] In this communication, we report observations that indicate the ferroelastic domains in bulk, polycrystalline γ-WO_3 have polar and photochemical properties similar to those of m-$BiVO_4$.[16]

Department of Materials Science and Engineering, Carnegie Mellon University, 5000 Forbes Ave., Pittsburgh, PA, 15213-3890, USA. E-mail: paulsalvador@cmu.edu

† Electronic supplementary information (ESI) available: A pdf including further details of standard experimental procedures, an XRD pattern, a BSE image identifying domain boundary orientation, further BSE images with spatially selective Ag^+, Pb^{2+}, and Mn^{2+} reactivity. See DOI: 10.1039/c7ta00842b

Sintered polycrystalline γ-WO_3 pellets were prepared by uniaxial pressing of WO_3 powder and subsequently annealing the green pellets at 1100 °C for 4 h. Their surfaces were ground and polished (the final polish was made using a 50 nm diamond suspension). Then the samples were annealed at 600 °C for 1 h to heal residual polishing damage. Details are given in the ESI.† X-ray diffraction results confirmed the samples were phase pure γ-WO_3 (Fig. S1†). A backscattered electron (BSE) image (experimental details are in the ESI†) from a single grain of WO_3 is given in Fig. 1(a). A clear hierarchical structure is observed in the contrast. Such domain structures are expected from γ-WO_3.[39–44] We assign three tiers to the domain structure, shown schematically in Fig. 1(b).

The widest domains run from the bottom left to the top right of Fig. 1(a). They alternate between dark and bright contrast, and they span the entire length of the image. We call these primary domains. Within any primary domain, another level of bright/dark contrast alternation is observed that spans the entire primary domain; we call these secondary domains. In this image, the secondary domain boundaries are oriented vertically (horizontally) in the darker (brighter) primary domains. They form a characteristic chevron pattern at the boundary of the primary domains. The third tier of contrast is associated with cross-hatched tweed and acicular patterns within the secondary domains; we call these tertiary domains. Within the brighter primary domains, a clear tweed (acicular) pattern is observed within the brighter (darker) secondary domains, (the acicular domains are not shown in the schematic in Fig. 1(b)). Within the darker primary domains, the tertiary domains are acicular, with the directions of the tertiary domains being rotated by ≈90° between the two secondary domains. Similar domain structures were observed for all grains (though tertiary domains were not always observed; we did not concentrate on characterizing the tertiary domains).

A BSE image from another region of the γ-WO_3 surface is shown in Fig. 2(a). Primary domains are visible in all grains, terminating at grain boundaries. Secondary domains are visible in most primary domains. A map of local orientations is given in Fig. 2(b) (for the same region as Fig. 2(a)), collected using electron backscatter diffraction (EBSD) (described in the ESI†). Different colors represent different values of the Euler angles in the $P2_1/c$ structure of γ-WO_3 (black pixels were unindexed). The colors alternate between related primary domains in Fig. 2(b), changing at the primary domain boundaries observed in Fig. 2(a). The changes in the crystallography across primary domains correspond to a rotation of ≈90° about the $\langle 100 \rangle_p$ and the domain boundary planes were consistent with $\{110\}_p$, where p indicates the use of pseudo-perovskite indices (an example is shown in Fig. S2†). These domains are consistent with expectations from the α–β (tetragonal to orthorhombic) transition (see ESI†).[33,39–41,43,48]

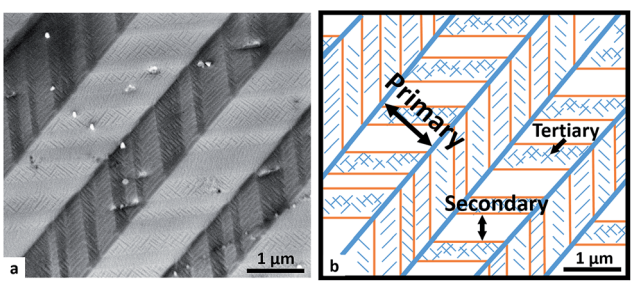

Fig. 1 (a) BSE image of the three-tier domain structure in a single grain. (b) Schematic of the domain structure. The bold solid blue lines indicate the primary domain walls. The thinner orange lines indicate the secondary domain walls. The tertiary domains are marked by thin solid blue lines within a secondary domain.

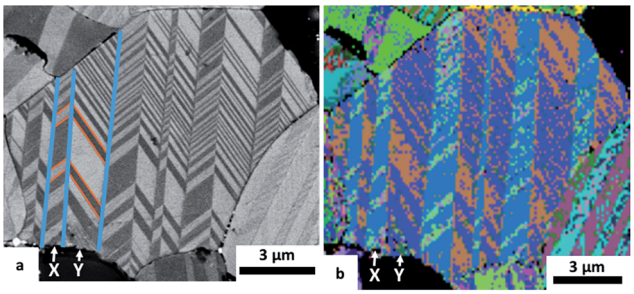

Fig. 2 (a) A BSE image and (b) a map of local Euler angles of a region of the γ-WO_3 surface. In (a), blue and orange lines mark some primary and secondary domain boundaries, respectively. In (b), different colors indicate different Euler angle values (crystallographic orientations). In both, X and Y mark the same primary domains.

The points within individual primary domains belong to one of two different colors, roughly correlating to the secondary domains observed in Fig. 2(a). In the central grain, the primary domains are purple/brown or blue/green. The secondary domains with dark contrast in Fig. 2(a) are approximately blue or purple in Fig. 2(b), and those with light contrast in Fig. 2(a) are generally green or brown in Fig. 2(b). That the secondary domains are not well resolved using automated EBSD is not surprising. First, the domains are all related by 90° rotations about $\langle 100 \rangle_p$ and, thus, the EBSD patterns are similar in these domains. Accurately differentiating the monoclinic distortion using standard indexing procedures employed here is challenging. Second, the existence of a tertiary domain structure (see Fig. 1(a)) would lead to multiple tertiary domains contributing to individual EBSD patterns, further complicating indexing. Nevertheless, pairs of secondary domains were found to be related through a rotation of ≈180° about the *a*- or *b*-axes, and the domain boundary directions (seen best in Fig. 2(a) and S2†) were found to be consistent with $\{100\}_p$ planes. Thus, the secondary domains are consistent with expectation from the β–γ (orthorhombic to monoclinic) transition[33,39–41,43,44,46,48,49] (the tertiary domain structure has been previously related to this transition[33,39–41,43,44,46,48,49]). The XRD, BSE, and EBSD patterns reinforce that these samples are consistent with bulk γ-WO_3.

A BSE image from an area on the surface that includes multiple grains is given in Fig. 3(a) and an out-of-plane piezoforce microscopy (PFM) phase image of the same region is given in Fig. 3(b). PFM contrast is observed in almost all grains, having a strong spatial correlation to the primary domains (Fig. 3(a)), though the contrast variation between primary

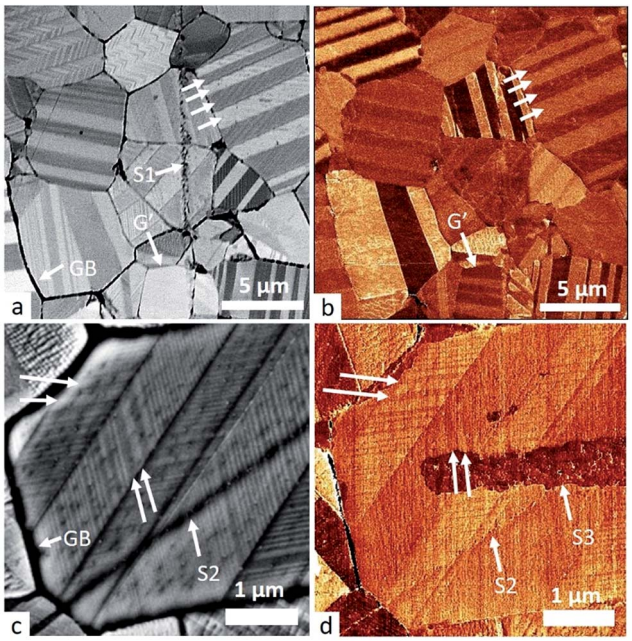

Fig. 3 (a) A BSE image showing domain structures in multiple grains. S1 (GB) indicates a scratch (grain boundary). (b) A PFM phase signal of the same area (vertical scale 20°). Arrows mark the same primary domains in (a) and (b). (c) A BSE image of a grain with primary and secondary domains. S2 (GB) indicates a scratch (grain boundary). (d) A PFM phase signal (vertical scale 23°) from the same grain, with S3 indicating a new scratch. Arrows mark the same secondary domains in (c) and (d).

domains varies greatly from grain to grain. Even when the primary domains yield negligible contrast in the BSE image (see grain G′), they can yield good contrast in the PFM image. The grains shown are representative of the entire population; PFM contrast is detectable for grains of all orientations (characterized using EBSD) and is strongly correlated with the primary domains observed in a BSE image. Kim *et al.*[47] previously reported that surfaces of heavily reduced single crystals of WO_3 are piezoresponsive. Yun *et al.*[44] reported that $\{100\}_p$ surfaces of epitaxial γ-WO_3 films were polar, with the PFM contrast correlating with their macro-domains (which had structure (sizes) similar to our primary (secondary) domains). Our observations indicate that polar surfaces appear to be general to γ-WO_3; they are not confined to specific orientations, epitaxies,[44] or reduction states of WO_3.[47]

BSE and out-of-plane PFM images of an individual grain with clear primary and secondary domains are given in Fig. 3(c) and (d), respectively. The secondary domains are rather fine, with widths between 50 and 150 nm. In the PFM images, these secondary domains also yield contrast, as indicated by several arrows (note the surface was scratched, marked as S3, during handling between BSE and PFM imaging). Thus, both primary and secondary domains have polar surfaces, and they can be resolved to a similar spatial extent as that observed in films.[44]

The surfaces of γ-WO_3 ceramics were used to photoreduce Ag^+ ions to insoluble Ag (see the ESI† for details). An out-of-plane PFM phase image is shown in Fig. 4(a) and a secondary

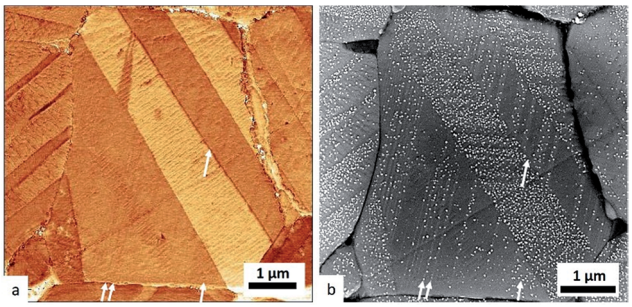

Fig. 4 (a) An out-of-plane PFM phase image (vertical scale of 37°) and (b) an SE image after the photochemical reduction of Ag^+, from the same area of γ-WO_3. White arrows point to the same secondary domains in (a) and (b).

electron (SE) image from the same region after photochemical reaction is shown in Fig. 4(b). As described before, strong (weak) PFM contrast is associated with primary (secondary) domains. Both crystallographic and topographic contrast are present in the SE image. The crystallographic contrast between secondary domains is relatively weak, but observable. Grey levels are relatively uniform within secondary domains. The topographic contrast from deposited Ag particles is strong and bright, and is overlaid on the weaker crystallographic contrast. Interestingly, the patterns of deposited Ag correlate with the patterns of PFM contrast. In the central grain, the two bright primary domains (that run up and to the left) are more reactive than the three dark domains. The reactivity within the primary domains also varies spatially and correlates with secondary domains observed clearly in the crystallographic contrast in Fig. 4(b) and faintly in the PFM images in the darker domains in Fig. 4(a) (shown by the white arrows). Two more SE images showing spatially selective reactivity are given in Fig. S4 and S5.†

The surfaces of γ-WO_3 ceramics were also used to photo-oxidize Pb^{2+} to PbO_2 (see the ESI† for details), and comparisons were made with the photo-reduction of Ag^+. An AFM topographic image and an out-of-plane PFM phase image are shown in Fig. 5(a) and (b) respectively, with two primary domains running nearly vertical in the image and secondary domains generating chevron patterns around the primary domain boundary. In this region, which has relatively wide secondary domains, the secondary domains exhibit strong contrast in the PFM image. AFM topographic images from the same location after photochemical Ag^+ reduction and Pb^{2+} oxidation are shown in Fig. 5(c) and (d), respectively. The topographic contrast from deposited Ag particles is strong and bright, with domains that have dark (bright) PFM contrast having dense and uniform (no or lower density) coverage of Ag particles. The topographic contrast from deposited PbO_2 particles is weaker than for the Ag particles, but spatially selective reactivity is clearly observed. Interestingly, the reactions are complementary: domains that are more (less) reactive for Ag^+ reduction are less (more) reactive for Pb^{2+} oxidation. This indicates that the surface polarization between these domains is significant enough to influence the near surface band bending to result in bifunctional surface reactivity: some

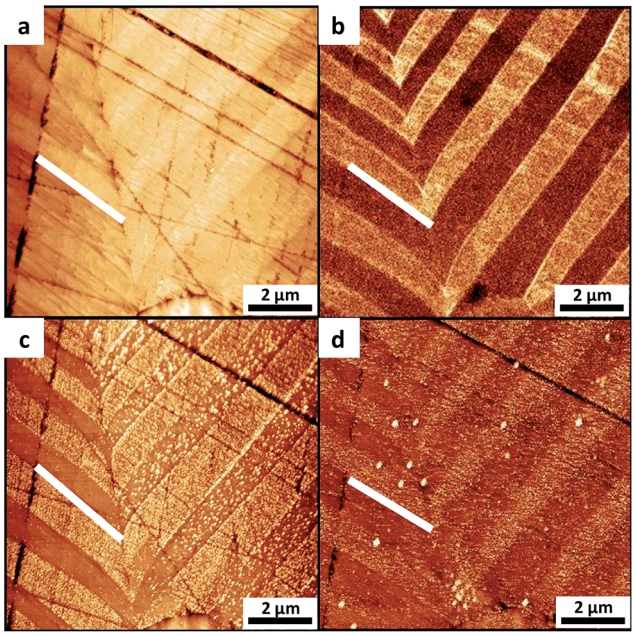

Fig. 5 (a) An AFM topographic image (vertical scale 40 nm) and (b) an out-of-plane PFM phase image (vertical scale 20°) of a WO_3 surface before reaction. AFM topographic images after (c) Ag and (d) PbO_2 photodeposition (with vertical scales of 50 and 60 nm respectively). White lines in each image indicate the same spatial location.

domains favour oxidation while others favour reduction. This type of complementary bifunctionality has been shown to be extremely beneficial for increasing the IQE of ferroelectrics, even for modest surface polarization values.[8,9]

Larger area SE images after Mn^{2+} and Pb^{2+} oxidation are shown in Fig. S6(a) and (b),† respectively. The patterns of photodeposited oxidation products in Fig. S6† correlate with the secondary domain patterns. They demonstrate that oxidation reactions are also correlated with the ferroelastic domain structure over all possible orientations. Collectively, the observations indicate that the surface of γ-WO_3 is spatially selective for both photocathodic and photoanodic reactions.

A different kind of spatially selective surface reactivity has been previously reported for γ-WO_3. The domain walls of γ-WO_3 are more reactive towards Na incorporation than the domains themselves, when surfaces are exposed to Na vapor.[38] Importantly, this modifies the domain wall properties compared to the bulk, even leading to the emergence of superconductivity at the domain walls owing to their selective doping.[50,51] In our work on γ-WO_3, the surface reactivity of domains themselves, and not the domain walls, are influenced by the domain's surface polarity. This leads to some domains being photocathodic and other being photoanodic, which are attractive attributes for efficient photocatalysts.

The ferroelastic domain selective reactivity of γ-WO_3 is analogous to that of m-$BiVO_4$.[15,16,52] For both materials, the orientation, domain structures, PFM response, and overall reactivity vary from grain to grain. Nevertheless, the patterns of photochemical reactivity, surface polarity, and ferroelastic domains are highly correlated. The reactivity of γ-WO_3 is correlated with both primary and secondary domain structures. Some primary domains are uniformly reactive (even when they have secondary domains) and some have reactivity correlated to the local secondary domain patterns. We were unable to resolve reactivity patterns dependent on tertiary domain structures, and the possibility that tertiary domains influence reactivity cannot be ruled out. Compared to m-$BiVO_4$, the hierarchical domain structure of γ-WO_3 adds a significant level of complexity to interpreting the observations.

Because both γ-WO_3 and m-$BiVO_4$ are centrosymmetric and non-polar, the origins of their polar surfaces and their coupling to the ferroelastic domain structure is unclear. In the absence of a structural model (which is beyond the scope of this communication), it is impossible to fully interpret the detailed patterns of polarity and surface reactivity observed. Flexoelectric effects were proposed as explanations of surface polarity in m-$BiVO_4$ [16] and γ-WO_3.[44] For γ-WO_3, however, stable polar phases have been reported to exist below room temperature,[30,53] and their stabilization at the surface owing to strain (or strain gradients) cannot be ruled out. These polar phases are energetically close to the ground state at room temperature.[35] Hence, their stabilization at strained surfaces is possible. Kim *et al.*[47] showed that the piezoresponsive surface of triclinic, reduced WO_3 had a structure distinct from the bulk. The existence of a polar surface phase would be consistent with the observations described here. Strain and strain gradients exist naturally at surfaces owing to thermal stresses on cooling and, in ferroelastics, to transformation stresses. They vary from grain to grain depending on the orientation and the local stress from neighboring grains. That both m-$BiVO_4$ and γ-WO_3 exhibit domain specific surface polarity and spatially selective photochemical reactivity indicates that these effects may be general to oxide ferroelastics.

While the surface polarization magnitude is unknown, it clearly impacts the reactivity of γ-WO_3 surfaces. The Ag^+ photoreduction occurs at locations having significant photogenerated electron populations. The counter-reaction (oxidation of water) occurs at locations having significant populations of photogenerated holes. Positive polar domains (*i.e.*, more positive surfaces) attract electrons and repel holes, while negative polar domains (*i.e.*, more negative surfaces) repel electrons and attract holes more than the non-polar baseline surfaces. The baseline reactivity is known to be orientation dependent for non-ferroelectric oxides,[54,55] including m-$BiVO_4$.[52] Differences in the relative magnitude of photochemical reactivity across grains likely arise from both orientation dependent reactivity and polarization driven modifications in the local reactivity, similar to m-$BiVO_4$.[52] For ferroelectrics, which have strong polar fields at the surface, the orientation dependence (polar dependence) is less (more) pronounced.[8,9,17,18] Importantly, it was shown that the polar ferroelastic surfaces of doped m-$BiVO_4$ were more photochemically active than the non-polar non-ferroelastic surfaces of similarly doped tetragonal $BiVO_4$.[15] Similar experiments are needed to demonstrate whether polar surfaces are more reactive than non-polar ones for γ-WO_3.

Conclusions

The domain structure at the surface of polished γ-WO_3 ceramics is hierarchical, having three levels of domains. For all orientations, the coarser two levels of domains (primary and secondary) are piezo-responsive (*i.e.*, polar). The spatially selective reactivity for photo-oxidation and photoreduction is correlated to the same two levels of ferroelastic domains that are piezoresponsive in PFM. These observations are similar to those reported for m-$BiVO_4$ and indicate that ferroelastics may be a general class of photocatalysts for which polar surfaces improve efficiencies.

Acknowledgements

The authors acknowledge the support of National Science Foundation grant DMR 1609369 and the use of the Materials Characterization Facility at CMU through grant MCF-677785.

Notes and references

1 S. Solomon, G. K. Plattner, R. Knutti and P. Friedlingstein, *Proc. Natl. Acad. Sci. U. S. A.*, 2009, **106**, 1704–1709.
2 S. J. Davis, K. Caldeira and H. D. Matthews, *Science*, 2010, **329**, 1330–1333.
3 S. Sharma and S. K. Ghoshal, *Renewable Sustainable Energy Rev.*, 2015, **43**, 1151–1158.
4 G. Collodi, *Chem. Eng. Trans.*, 2010, **19**, 37–42.
5 A. Fujishima and K. Honda, *Nature*, 1972, **238**, 37–38.
6 R. Sathre, C. D. Scown, W. R. Morrow III, J. C. Stevens, I. D. Sharp, J. W. Ager III, K. Walczak, F. A. Houle and J. B. Greenblatt, *Energy Environ. Sci.*, 2014, **7**, 3264–3278.
7 S. R. Morrison, *Electrochemistry at Semiconductor and Oxidized Metal Electrodes*, Plenum Press, New York, 1980.
8 J. J. Glickstein, P. A. Salvador and G. S. Rohrer, *J. Mater. Chem. A*, 2016, **4**, 16085–16093.
9 J. J. Glickstein, P. A. Salvador and G. S. Rohrer, *J. Phys. Chem. C*, 2016, **120**, 12673–12684.
10 *Ferroelectricity: The Fundamentals Collection*, ed. J. A. Gonzalo and B. Jiménez, Wiley-VCH, Weinheim, 2008.
11 P. S. Halasyamani and K. R. Poeppelmeier, *Chem. Mater.*, 1998, **10**, 2753–2769.
12 F. G. Wang, I. Grinberg and A. M. Rappe, *Appl. Phys. Lett.*, 2014, **104**, 152903.
13 J. G. He, C. Franchini and J. M. Rondinelli, *Chem. Mater.*, 2016, **28**, 25–29.
14 A. M. Schultz, Y. Zhang, P. A. Salvador and G. S. Rohrer, *ACS Appl. Mater. Interfaces*, 2011, **3**, 1562–1567.
15 R. Munprom, P. A. Salvador and G. S. Rohrer, *J. Mater. Chem. A*, 2016, **4**, 2951–2959.
16 R. Munprom, P. A. Salvador and G. S. Rohrer, *Chem. Mater.*, 2014, **26**, 2774–2776.
17 J. L. Giocondi and G. S. Rohrer, *Chem. Mater.*, 2001, **13**, 241–242.
18 J. L. Giocondi and G. S. Rohrer, *J. Phys. Chem. B*, 2001, **105**, 8275–8277.
19 P. Zubko, G. Catalan and A. K. Tagantsev, *Annu. Rev. Mater. Res.*, 2013, **43**, 387–421.
20 Z. Zhao, X. Ding, J. Sun and E. K. H. Salje, *J. Phys.: Condens. Matter*, 2014, **26**, 142201.
21 A. Kudo, K. Ueda, H. Kato and I. Mikami, *Catal. Lett.*, 1998, **53**, 229–230.
22 S. Tokunaga, H. Kato and A. Kudo, *Chem. Mater.*, 2001, **13**, 4624–4628.
23 K. Maeda and K. Domen, *J. Phys. Chem. Lett.*, 2010, **1**, 2655–2661.
24 W. Erbs, J. Desilvestro, E. Borgarello and M. Gratzel, *J. Phys. Chem.*, 1984, **88**, 4001–4006.
25 G. R. Bamwenda and H. Arakawa, *Appl. Catal., A*, 2001, **210**, 181–191.
26 I. M. Szilagyi, B. Forizs, O. Rosseler, A. Szegedi, P. Nemeth, P. Kiraly, G. Tarkanyi, B. Vajna, K. Varga-Josepovits, K. Laszlo, A. L. Toth, P. Baranyai and M. Leskela, *J. Catal.*, 2012, **294**, 119–127.
27 R. Liu, Y. J. Lin, L. Y. Chou, S. W. Sheehan, W. S. He, F. Zhang, H. J. M. Hou and D. W. Wang, *Angew. Chem., Int. Ed.*, 2011, **50**, 499–502.
28 E. Salje and K. Viswanathan, *Acta Crystallogr., Sect. A: Cryst. Phys., Diffr., Theor. Gen. Crystallogr.*, 1975, **31**, 356–359.
29 R. A. Dixon, J. J. Williams, D. Morris, J. Rebane, F. H. Jones, R. G. Egdell and S. W. Downes, *Surf. Sci.*, 1998, **399**, 199–211.
30 P. M. Woodward, A. W. Sleight and T. Vogt, *J. Solid State Chem.*, 1997, **131**, 9–17.
31 T. Vogt, P. M. Woodward and B. A. Hunter, *J. Solid State Chem.*, 1999, **144**, 209–215.
32 E. Salje, *Acta Crystallogr., Sect. A: Cryst. Phys., Diffr., Theor. Gen. Crystallogr.*, 1975, **31**, 360–363.
33 J. A. Perri, E. Banks and B. Post, *J. Appl. Phys.*, 1957, **28**, 1272–1275.
34 K. R. Locherer, I. P. Swainson and E. K. H. Salje, *J. Phys.: Condens. Matter*, 1999, **11**, 6737–6756.
35 H. Hamdi, G. Philippe and B. Eric, *Phys. Rev. B*, 2016, **94**, 245124.
36 K. R. Locherer, I. P. Swainson and E. K. H. Salje, *J. Phys.: Condens. Matter*, 1999, **11**, 4143–4156.
37 C. J. Howard, V. Luca and K. S. Knight, *J. Phys.: Condens. Matter*, 2002, **14**, 377–387.
38 A. Aird and E. K. H. Salje, *Eur. Phys. J. B*, 2000, **15**, 205–210.
39 R. Ueda and T. Ichinokawa, *J. Phys. Soc. Jpn.*, 1951, **6**, 122–123.
40 S. Tanisaki, *J. Phys. Soc. Jpn.*, 1958, **13**, 363–366.
41 S. Sawada and G. C. Danielson, *Phys. Rev.*, 1959, **113**, 1005–1008.
42 F. Uchikoba and K. Sawamura, *J. Am. Ceram. Soc.*, 1994, **77**, 1345–1351.
43 R. G. Rhodes, *Nature*, 1952, **170**, 369.
44 S. Yun, C. S. Woo, G. Y. Kim, P. Sharma, J. H. Lee, K. Chu, J. H. Song, S. Y. Chung, J. Seidel, S. Y. Choi and C. H. Yang, *Appl. Phys. Lett.*, 2015, **107**, 252904.
45 S. I. Hamazaki, N. Tashiro, Y. Fukurai, F. Shimizu, M. Takashige and S. Kojima, *Ferroelectrics*, 1998, **219**, 819–825.

46 S. Hamazaki, N. Tashiro, F. Shimizu and M. Takashige, *J. Phys. Soc. Jpn.*, 1998, **67**, 2144–2145.
47 Y. Kim, A. Marin and E. K. H. Salje, *Appl. Phys. Lett.*, 2010, **96**, 032904.
48 J. Sapriel, *Phys. Rev. B: Solid State*, 1975, **12**, 5128–5140.
49 S. Hamazaki, N. Tashiro, F. Shimizu, S. Sawada and M. Takashige, *Ferroelectrics*, 1999, **231**, 631–635.
50 A. Aird and E. K. H. Salje, *J. Phys.: Condens. Matter*, 1998, **10**, L377–L380.
51 A. Aird, M. C. Domeneghetti, F. Mazzi, V. Tazzoli and E. K. H. Salje, *J. Phys.: Condens. Matter*, 1998, **10**, L569–L574.
52 R. Munprom, P. A. Salvador and G. S. Rohrer, *J. Mater. Chem. A*, 2015, **3**, 2370–2377.
53 E. K. H. Salje, S. Rehmann, F. Pobell, D. Morris, K. S. Knight, T. Hermannsdorfer and M. T. Dove, *J. Phys.: Condens. Matter*, 1997, **9**, 6563–6577.
54 J. L. Giocondi and G. S. Rohrer, *J. Am. Ceram. Soc.*, 2003, **86**, 1182–1189.
55 Y. Zhu, P. A. Salvador and G. S. Rohrer, *J. Am. Ceram. Soc.*, 2016, **99**, 2428–2435.

Journal Name

COMMUNICATION

Supplemental Information to:

Spatial selectivity of photodeposition reactions on polar surfaces of centrosymmetric ferroelastic γ-WO_3†

Received 00th January 20xx,
Accepted 00th January 20xx

DOI: 10.1039/x0xx00000x

www.rsc.org/MaterialsA

Ajay S. Pisat, Gregory S. Rohrer, and Paul A. Salvador*

This pdf document contains details of WO_3 sample preparation, x-ray diffraction, electron microscopy methods, identification of crystallographic orientation of domain boundaries, piezoforce microscopy, and photochemical marker reactions. It contains a table of polishing procedures (Table S1) and figures of: experimental and simulated x-ray diffraction patterns (Fig. S1), backscatter electron image of the multilevel domain structure and related crystallography (Fig. S2), schematic of photochemical marker reactions (Fig. S3), and examples of secondary electron images of Ag coated (Fig. S4 and S5) and PbO_2 or MnO_2 coated (Fig. S6) surfaces after photochemical marker reactions.

1. Preparation of γ-WO_3 samples

Commercial WO_3 powder (99.9%, Sigma Aldrich) was used throughout this work. The powder was wet ground in acetone using a mortar and pestle for 5 min. 2 g of ground powder was then mixed with a drop of polyvinyl alcohol as a binder and cold-pressed into a pellet using a tabletop hydraulic press (Carver). Pressed pellets were then sintered in an alumina crucible. The pellets were laid on a bed of WO_3 powder to prevent direct reaction with the alumina during sintering. The pellets were fired at 1100 °C for 4 h using a ramp rate of 10 °C/min for heating and cooling. On cooling, the pellets go through the α–β (740 °C) and β–γ (310 °C) transformations.

One side of a given pellet was polished to a mirror finish. Polishing was carried out on a Buehler Automet 250 machine, with a head cadence of 60 revolution per minute (rpm) and a force of 1 lb. Details of the polishing steps are given in Table S1. After polishing, the pellets were annealed at 600 °C for 1 h, heating at 5 °C/min and cooling at 10 °C/min, to heal polishing damage at the surface. It should be noted that this thermal cycling goes through the β–γ (310 °C) transformation. Prior to further surface analysis, polished pellets were sonicated successively in acetone, ethanol, and DI water for 3 min each.

Table S1: Recipe for polishing the sintered WO_3 pellets

Step number	Base speed[a]	Polishing paper/cloth + suspension	Time[a]
1	120	320 grit Carbimet	0.5
2	120	600 grit Carbimet	1
3	120	800 grit Carbimet	1.5
4	150	1200 grit Carbimet	2
5	180	Satyn MB + 9 µm diamond suspension	3
6	180	Satyn MB + 3 µm diamond suspension	4
7	180	Satyn MB + 1 µm diamond suspension	5
8	200	Micro MB + 0.05 µm diamond suspension	8

[a] Base speed is given in rpm and time in min.

2. X-ray Diffraction (XRD)

One polished pellet was ground using a mortar and pestle for x-ray diffraction (XRD) analysis. The powder was spread on a glass slide and mounted in an X'Pert Pro MPD x-ray diffractometer. XRD was carried out using 45 kV and 40 mA with a Cu target (radiation wavelength 1.54 Å). Θ-2Θ patterns were collected, registering XRD intensity every 0.026 ° from 20 – 65 ° at a speed of 0.067 °/s. An x-ray diffractogram for γ-WO_3 was simulated using CrystalDiffract[1] software for comparison with the acquired patterns. The structural parameters for γ-WO_3 were taken from Loopstra and Rietveld.[2]

In Fig. S1, the experimental XRD pattern is given as the upper curve and the simulated pattern is given as the lower curve. The number and position of peaks in the experimental pattern were well matched to peaks in the simulated pattern, though the relative intensities varied between peaks in the two patterns. The simulated pattern assumes a perfectly random mixture of orientations with identical grain sizes and shape, which is not likely true in the experimental powder. The similarity of the patterns (and the dis-similarity to other polymorphs, not shown) support the conclusion that the sample is γ-WO_3.

*Department of Materials Science and Engineering, Carnegie Mellon University, 5000 Forbes Ave., Pittsburgh, PA, 15213-3890, USA: Email: *Email - paulsalvador@cmu.edu*

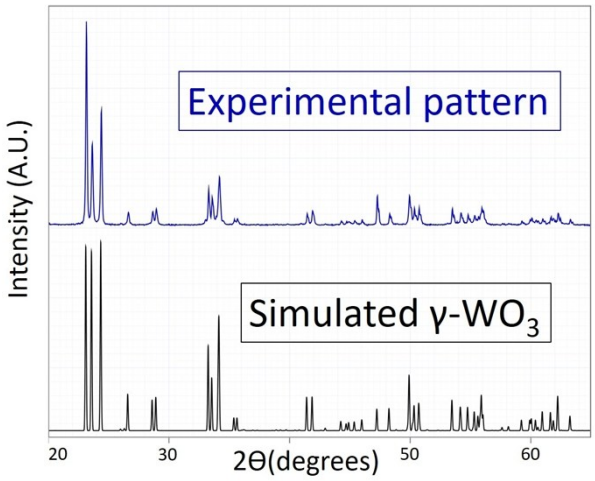

Fig. S1: Comparison of the experimental and simulated XRD patterns.

3. Backscatter electron (BSE) imaging

BSE imaging was carried out using an FEI Quanta 200 FEG (field emission gun) and an FEI Quanta 600 FEG scanning electron microscope (SEM). Accelerating voltages ranged from 5 to 15 kV. The spot size was typically 4 or 5, but 3.5 was used for improved imaging of tertiary domains. The contrast was set to 80-90 % of the maximum possible value while the brightness was set to 0-15 % of the maximum possible value. The image acquisition times ranged from 3-6 minutes per image to achieve the desirable quality (i.e., signal-to-noise ratio). Image resolution was 1024 x 884. Contrast between domains arises from differences between electron counts from differences in electron channeling in different domains.

Similar domain structures to those given in various figures throughout the main text and SI were observed for all grains. Primary and secondary domains were almost always evident, but tertiary domains were not consistently imaged. The tertiary domains are at the limit of the microscope's resolution and their appearance is sensitive to their local character and to imaging conditions. The lack of contrast from domains in a given BSE image does not rule out their presence. We did not concentrate on characterizing the tertiary domains.

4. Electron Backscatter Diffraction (EBSD)

EBSD was carried out using an FEI Quanta 600 FEG SEM equipped with an Oxford HKL EBSD system and an HKL NordlysNano camera. The accelerating voltage was 20 kV. The sample was mounted on a pre-tilted sample holder (70°). Patterns were collected using a dwell time between 140 and 200 ms per frame and averaging two frames together for the final pattern.

The patterns were then indexed using two variations of the space group No. 14: $P2_1/c$ and $P2_1/n$. In the $P2_1/c$ system, the cell parameters used were a = 7.69 Å, b = 7.54 Å, c= 10.525 Å and β = 136.05° (calculated from the P $2_1/n$ values given below). This setting was used to resolve crystallographic orientation differences for the secondary domains (shown in Fig. 2(b)). In the $P2_1/n$ system, the cell parameters were a = 7.36 Å, b = 7.54 Å, c = 7.69 Å and β = 90.9°.[2] This setting corresponds well to the (doubled) pseudo-perovskite unit cell, and we used it to simplify the categorization of the primary and secondary domain wall crystallography (which we describe relative to the cubic system below).

5. Identification of Domain walls

The observed domain structures (see main text) have two characteristic features: primary domains that span the length of the grain and secondary domains that span the width of their corresponding primary domain. The hierarchical structure suggests that the primary structure might form as a result of the α-WO_3 (tetragonal) to β-WO_3 (orthorhombic) transition that occurs when the sample is cooled below 740 °C after synthesis and that the secondary structure might form as a result of the β-WO_3 (orthorhombic) to γ-WO_3 (monoclinic) transition that occurs when the sample is cooled below 310 °C (on cooling from the post-polishing anneal).

To identify the crystallography associated to primary and secondary domain boundaries, we studied grains that had the *a*, *b*, or *c* axes oriented within 10° of the surface normal, based on the $P2_1/n$ EBSD data. The $P2_1/n$ monoclinic γ-WO_3 structure can be most easily understood as a distorted doubled perovskite with the A-sites completely empty.[3] Because all polymorphs can be related to the cubic pseudo-perovskite subcell, we used the data in the $P2_1/n$ setting to describe the crystallography. Fig. S2 shows a BSE image of a grain whose primary domains have the [100] or [010] axes normal to the surface plane. Below the image, the crystal axes are show for two domains (indicated by arrows).

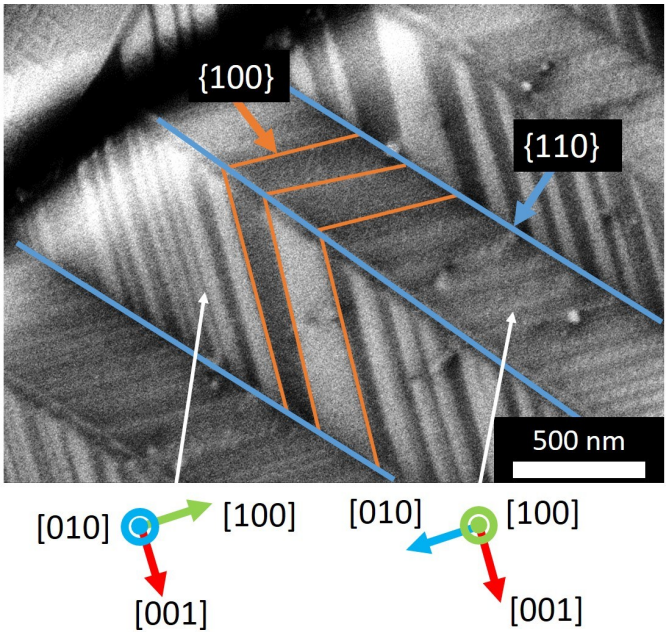

Fig. S2: BSE image of a grain showing two levels of domains. The Blue lines indicate the primary domain boundaries. The orange lines indicate the secondary domain boundaries. The orientations of the primary domains as indexed in the P $2_1/n$ (pseudo-perovskite) system are indicated by the coordinate systems shown below.

Using the Euler angles of the primary domains, we determined the angles that the traces of planes in the {110} and {100} families would make with the surface plane. The calculated traces were then matched with the observed traces using ImageJ.[4] The traces of the (-101) and (011) planes (according to the two different coordinate systems of the two different primary domains), are depicted in blue in Fig. S2 (marked as {110}). These align well with the primary domain boundaries. The traces of the (100) and (001) planes (according to the two different coordinate systems of the two different primary domains), are depicted in orange in Fig. S2 (marked as {100}). These align well with the secondary domain boundaries. The measured angle between the traces of the secondary domain boundaries is 90 ± 1°, consistent with the expected angle between the traces of the (100) and (001) planes.

Similar analyses were carried out for several grains. In the cases investigated, the primary domain boundaries were consistent with $\{110\}_p$ planes and the secondary boundaries with $\{100\}_p$ planes, where the subscript *p* denotes these are given using the cubic pseudo-perovskite indexes. Further, the rotation across the primary domains was usually 90° about the $<100>_p$ and the rotation about the secondary domains were 180 ° about another $<100>_p$ direction. These types of planes are commonly observed as domain boundaries in WO_3. [5-13]

Following Sapriel's[24] analysis suggests that domains formed as a result of the tetragonal to orthorhombic ferroelastic transition should have domain walls along x = y or x = -y. In γ-WO_3 terms, this means the domains associated with the α to β (tetragonal to orthorhombic) transformation could lie along the $\{110\}_p$ planes, which is consistent with the primary domain boundaries. Sapriel's[24] analysis also suggests that domains formed as a result of the orthorhombic to monoclinic ferroelastic transition should have domain boundaries along x=0 and z=0, which implies walls along (001) or (100), which are consistent with the secondary domains.

Thus, the primary domains, which span entire grains, are consistent with expectations from the α to β (tetragonal to orthorhombic) transition (at 740 °C).[5-10] The secondary and tertiary domains are consistent with the β to γ (orthorhombic to monoclinic) transition (at 310 °C).[5-13] These observations are also consistent with the domain boundary planes reported by Tanisaki[26] on single crystals of WO_3.

6. Piezoforce Microscopy (PFM)

Piezoforce Microscopy (PFM) was carried out using an NT-MDT Solver NEXT tabletop AFM. The samples were cleaned in acetone, ethyl alcohol, and distilled water, and then wiped with a methanol soaked Kimwipe (KimTech) before being imaged in the AFM. Conductive probes by Nanoworld (ARROW-EFM: cantilever frequency = 75 kHz, spring constant = 2.8 N/m, cantilever length = 240 µm) were used. A scanning speed of 3 µm/s was used, with an AC bias of 4 V. The AC frequency used was approximately 320 kHz, where the first contact resonance was observed. As described in the main text, the PFM contrast correlated well with the primary and secondary domain structures. We did not resolve if (or how) the surface polarity was related to the tertiary domain structure.

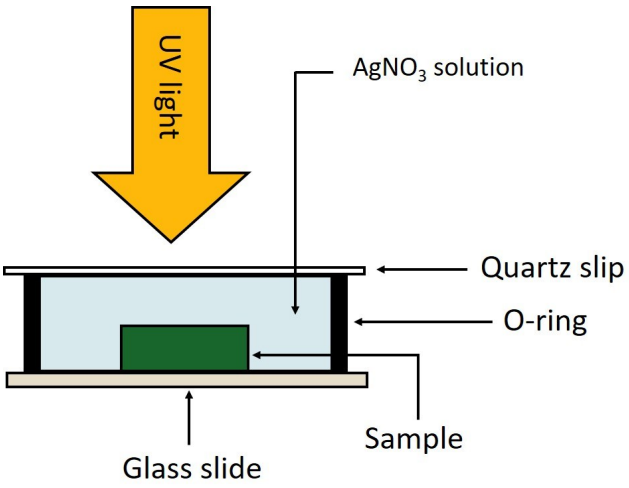

Fig. S3: Schematic of the setup for carrying out photochemical marker reactions.

7. Photochemical Ag^+ reduction

The setup used for photodeposition reactions (the marker reactions) is schematized in Fig. S3. The sample was attached to a glass slide using double sided tape. A rubber O-ring was placed upon the glass slide surrounding the sample. An appropriate solution was filled up to the brim of the O-ring, which was then covered with a thin quartz slip. The quartz slip was used to allow complete transmission of UV light while retaining the solution within the O-ring. For Ag^+ reduction, a 0.115 M solution of $AgNO_3$ was used, prepared by dissolving 0.097 g of $AgNO_3$ in 5 ml of distilled water. For Pb^{+2} (Mn^{2+}) photo-oxidation, a 0.345 M solution of $Pb(CH_3COO)_2$ (0.345 M solution of $MnSO_4$-$4H_2O$) was used, prepared by dissolving 0.561 g of $Pb(CH_3COO)_2$ (0.384 g of $MnSO_4$-$4H_2O$) in 5 ml of distilled water.

The Ag^+ photoreduction (Pb^{2+}/Mn^{2+} photo-oxidation) reactions were carried out by exposing the above setup to UV light with a power of 75 W for 6 s (150 W for 180 s). The incident UV light excites electrons in the sample to the conduction band, leaving holes in the valence band. The photogenerated carriers move to the solution-sample interface where one carrier reacts with the metal ions to form water-insoluble deposits of Ag, PbO_2, or MnO_2, while the other carrier reacts with water. After photochemical reaction, the sample was cleaned of excess solution by carefully dipping it in distilled water 10 times. The sample surface was then dried using a 99.99 % pure nitrogen stream.

Secondary electron (SE) imaging of samples after marker reactions was carried out using the FEI Quanta 600 at 20 kV with a spot size of 4. The acquisition time for each image was 3-6 min. Longer times were necessary to image finer silver particles (sizes ≈ 50 nm) on domains. SE images are given in Figs S4, S5, and S6.

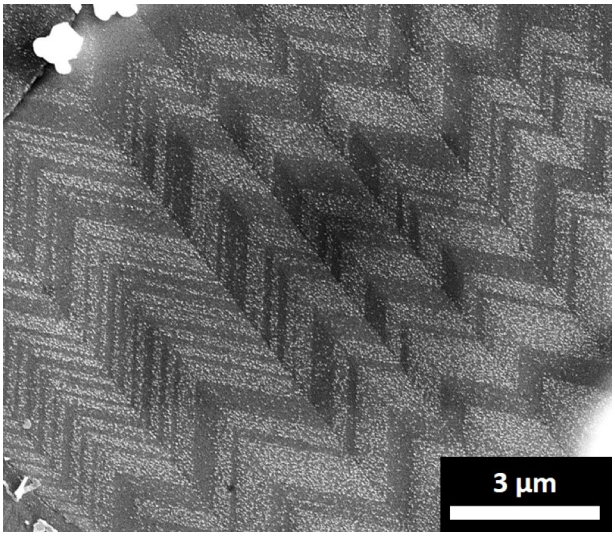

Fig. S4. An SE image of domain specific photochemical Ag^{+} reduction on the surface of the WO_3.

The topographic contrast from deposited particles shows up as bright contrast in Figs S4, S5, and S6. The contrast from Ag particles is overlaid on the weaker crystallographic contrast (see main text), the latter of which is more readily observable in Fig. S5 (at the higher magnification). The patterns of deposited Ag in Fig. S4 and S5 correlate with the secondary domain patterns as observed in BSE, EBSD, and PFM images given in the main text and SI. In Fig. S4, clear chevron patterns are observed, with some secondary domains covered densely with Ag particles and others covered sparsely. In Fig. S5, four bright primary domains (that run up and to the left at a shallow angle) are more reactive than the four dark domains. Within the reactive primary domain, the silver particles seem to be ordered into lines (that run up and to the left at a steep angle). These lines traverse the primary domains in a similar pattern to the expectation of secondary domains.

Photo-oxidation of Pb^{2+} and Mn^{2+} to insoluble PbO_2 and MnO_2 were also carried out on the WO_3 surfaces. SE images after Mn^{2+} and Pb^{2+} oxidation are shown in Fig. S6(a) and (b), respectively. The patterns of photodeposited products in Fig. S6 again correlate with the secondary domain patterns as observed in BSE, EBSD, and PFM images given in the main text and SI, indicating that oxidation reactions are also correlated with the ferroelastic domain structure of WO_3, especially the primary and secondary domains. An example of complementary reactivity on WO_3 is shown in Fig. 5 of the main text.

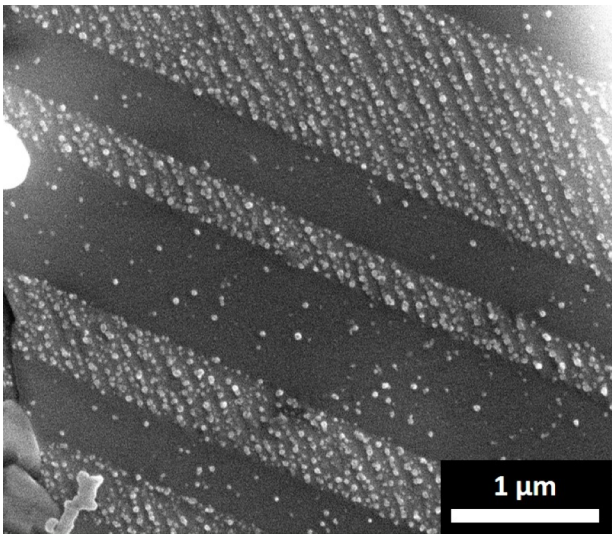

Fig. S5. An SE image of domain specific photochemical Ag^{+} reduction on the surface of the WO_3.

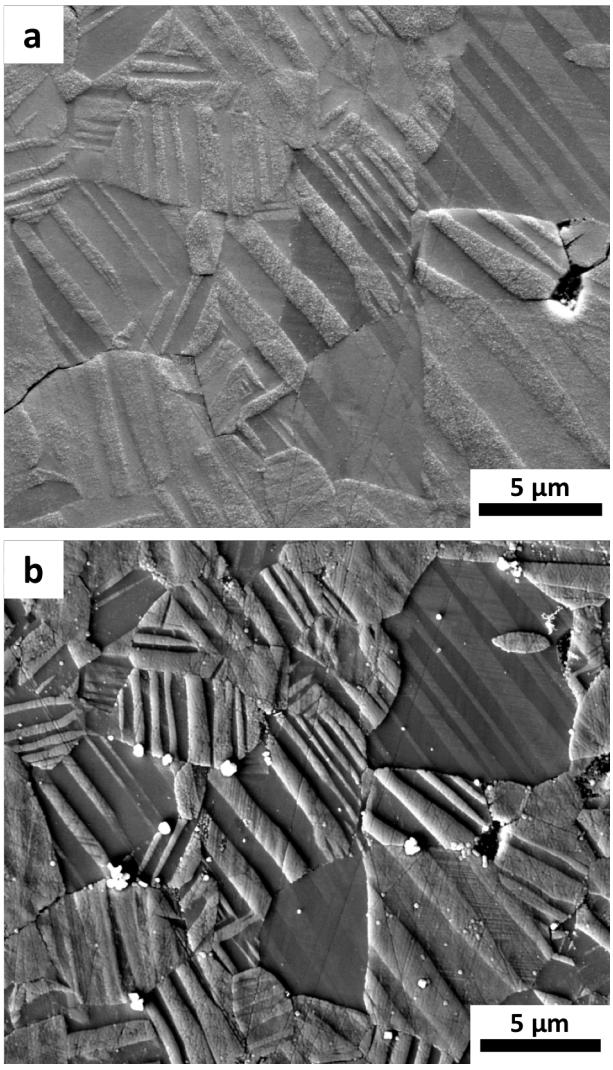

Fig. S6. SE image of domain specific photochemical oxidation of (a) Mn^{2+} and (b) Pb^{2+} on the surface of the WO_3.

Notes and references

1 Simulated XRD patterns were generated using CrystalMaker® (v.9) and CrystalDiffract® (v.6). http://www.crystalmaker.com/ , http://crystalmaker.com/crystaldiffract/, 2016).
2 B. O. Loopstra and H. M. Rietveld, *Acta Crystallographica B*, 1969, **25**, 1420-1421.
3 T. Vogt, P. M. Woodward and B. A. Hunter, *J. Solid State Chem.*, 1999, **144**, 209-215.

4 C. A. Schneider, W. S. Rasband and K. W. Eliceiri, *Nat Methods*, 2012, **9**, 671-675.
5 R. Ueda and T. Ichinokawa, *J. Phys. Soc. Jpn.*, 1951, **6**, 122-123.
6 R. G. Rhodes, *Nature*, 1952, **170**, 369-369.
7 J. A. Perri, E. Banks and B. Post, *J. Appl. Phys.*, 1957, **28**, 1272-1275.
8 S. Tanisaki, *J. Phys. Soc. Jpn.*, 1958, **13**, 363-366.
9 S. Sawada and G. C. Danielson, *Phys. Rev.*, 1959, **113**, 1005-1008.
10 J. Sapriel, *Phys. Rev. B*, 1975, **12**, 5128-5140.
11 S. Hamazaki, N. Tashiro, F. Shimizu and M. Takashige, *J. Phys. Soc. Jpn.*, 1998, **67**, 2144-2145.
12 S. Hamazaki, N. Tashiro, F. Shimizu, S. Sawada and M. Takashige, *Ferroelectrics*, 1999, **231**, 631-635.
13 S. Yun, C. S. Woo, G. Y. Kim, P. Sharma, J. H. Lee, K. Chu, J. H. Song, S. Y. Chung, J. Seidel, S. Y. Choi and C. H. Yang, *Appl. Phys. Lett.*, 2015, **107**.